

# Fourier-Domain Beamforming and Structure-Based Reconstruction for Plane-Wave Imaging

Tanya Chernyakova<sup>1</sup>, *Student Member, IEEE*, Regev Cohen<sup>1</sup>, *Student Member, IEEE*, Rotem Mulayoff,  
Yael Sde-Chen, Christophe Fraschini, Jeremy Bercoff, and Yonina C. Eldar<sup>2</sup>, *Fellow, IEEE*

**Abstract**—Ultrafast imaging based on coherent plane-wave compounding is one of the most important recent developments in medical ultrasound. It significantly improves the image quality and allows for much faster image acquisition. This technique, however, requires large computational load motivating methods for sampling and processing rate reduction. In this work, we extend the recently proposed frequency-domain beamforming (FDBF) framework to plane-wave imaging. Beamforming in frequency yields the same image quality while using fewer samples. It achieves at least fourfold sampling and processing rate reduction by avoiding oversampling required by standard processing. To further reduce the rate, we exploit the structure of the beamformed signal and use compressed sensing methods to recover the beamformed signal from its partial frequency data obtained at a sub-Nyquist rate. Our approach obtains tenfold rate reduction compared with standard time-domain processing. We verify performance in terms of spatial resolution and contrast based on the scans of a tissue mimicking the phantom obtained by a commercial Aixplorer system. In addition, *in vivo* carotid and thyroid scans processed using standard beamforming and FDBF are presented for qualitative evaluation and visual comparison. Finally, we demonstrate the use of FDBF for shear-wave elastography by generating velocity maps from the beamformed data processed at sub-Nyquist rates.

**Index Terms**—Array processing, beamforming compressed sensing (CS), plane wave, ultrasound.

## I. INTRODUCTION

ULTRASOUND is a radiation-free imaging modality with numerous applications. The image is usually comprised of multiple scanlines, obtained by sequential insonification of the medium using focused acoustic beams. Thus, in most commercial systems today, the number of transmissions is dictated by the number of scanlines comprising the image. As a result, the frame rate is limited to several tens of frames per second, which is insufficient for a number of applications including echocardiography for heart motion analysis, 3-D/4-D imaging, and elastography.

Manuscript received June 17, 2018; accepted July 9, 2018. Date of publication July 16, 2018; date of current version October 3, 2018. This work was supported by the European Union's Horizon 2020 Research and Innovation Program under Grant 646804-ERC-COG-BNYQ. (Tanya Chernyakova and Regev Cohen contributed equally to this work.) (Corresponding author: Tanya Chernyakova.)

T. Chernyakova, R. Cohen, R. Mulayoff, Y. Sde-Chen, Y. C. Eldar are with the Department of Electrical Engineering, Technion-Israel Institute of Technology, Haifa 3200003, Israel (e-mail: ctanya@campus.technion.ac.il).

C. Fraschini and J. Bercoff are with Supersonic Imagine, 13857 Aix-en-Provence, France.

Digital Object Identifier 10.1109/TUFFC.2018.2856301

The key to frame rate improvement without compromising the image quality is to break the link between the number of transmissions and the number of scanlines. An obvious way to reduce the number of transmissions is to insonify the entire scene with a pulsed plane wave. The image lines are then obtained in parallel from the acquired data by standard dynamic beamforming upon reception. This approach was successfully applied by Sandrin *et al.* [1] and Bercoff *et al.* [2] for real-time elastography, namely, imaging of the propagation of shear mechanical waves, implying ultrafast frame rates. However, due to the inherent lack of focusing upon transmission, this method suffers from reduced contrast and resolution. One approach to overcome this limitation is by sequential transmission of several tilted plane waves [3]. The images obtained from each insonification are added coherently to yield a final compounded image. The result is characterized by significantly improved resolution and contrast, since coherent compounding effectively generates *a posteriori* synthetic focusing in the transmission [3].

Coherent plane-wave compounding provides a framework for significant frame rate reduction while retaining the image quality. This method, however, is challenging due to the high data transfer rates and large computational load. To achieve ultrafast imaging, all image lines are computed in parallel, typically on a software-based platform. This implies that sampled raw radio-frequency (RF) signals, detected at each array element, are directly transferred to the processing unit. Each image line is obtained by standard time-domain beamforming, implying sampling rates that are much higher than the Nyquist rate of the detected signals. Rates up to 4–10 times the central frequency of the transmitted pulse are used in order to eliminate artifacts caused by digital implementation of beamforming in time [4]. Considering the number of transducer elements, up to  $10^7$  samples, needs to be transferred and digitally processed in real time to obtain an image. The processing unit, therefore, must be powerful enough to allow for real-time beamforming.

One approach to reduce sampling rate is by quadrature sampling [5]. Here, the signals are sampled at rates dictated by the RF Nyquist condition and then digitally demodulated and decimated to the effective Nyquist rate defined by the signals' bandpass bandwidth. The resulting in-phase ( $I$ ) and quadrature ( $Q$ ) components are then used for further processing. Digital IQ demodulation and decimation require multiplication by complex exponentials and low-pass filtering of

each sampled signal, thus increasing the overall computational load. Moreover, elastography, one of the main applications of ultrafast imaging, requires RF ultrasound data for tissue deformation calculations [6]–[8]. Therefore, alternatives for sampling and processing rate reduction are of high interest and can lead to simpler and cheaper systems. They may also serve as a potential enabler for the concept of a wireless probe and remote processing [9].

#### A. Related Work

In the focused mode, a number of strategies exploiting the signal structure and relying on compressed sensing (CS) techniques [10], [11] have been proposed for data rate reduction. These methods either allow for sampling and recovery of each individual detected signal at a low rate assuming sufficiently high SNR [12]–[15] or deal with recovering a beamformed signal from its low-rate samples [16]–[19]. The latter requires access to the continuous-time beamformed data, while, in practice, the beamformed signal is formed digitally at a high rate from the samples of each of the individual received signals.

A practical method to acquire low-rate beamformed data from the low-rate samples of the received signals in order to visualize macroscopic perturbations in the tissue was first suggested in [20] and was later extended to ultrafast imaging in [21]. A significant drawback of this approach is that the solution is approximated using the orthogonal matching pursuit that fails to restore weak reflectors and leads to loss of speckle [22]. An improved technique, enabling sub-Nyquist data acquisition from each transducer element and low-rate processing, was presented in [22] to visualize all tissue components, namely, both strong reflectors and weak scattered echoes. A generalization to 3-D imaging was proposed in [23].

This sub-Nyquist approach is based on frequency-domain beamforming (FDBF) where the computations can be carried out from less data samples. The Fourier components of the beamformed signal are computed as a weighted average of those of the individual detected signals. The weights are obtained through a distortion function that transfers the non-linear time-dependent beamforming delays to the frequency domain. Since the beam is obtained directly in frequency, its Fourier components are computed only within its effective bandwidth. When all the beam's Fourier coefficients within its bandwidth are computed, the sampling and processing rates are equal to the effective Nyquist rate [10]. In this case, the oversampling required by the time-domain implementation of digital beamforming [4] is avoided leading to 4–10-fold rate reduction. The beam in time is then recovered by an inverse Fourier transform.

When further rate reduction is required, only a subset of the beam's Fourier coefficients is obtained, implying that the detected signals are sampled and processed at a sub-Nyquist rate. Recovery then relies on CS methods that exploit an appropriate model of the beam to compensate for the lack of frequency data. Low-rate data acquisition is based on the ideas of Xampling [12], [24], [25], which obtains the Fourier coefficients of individual detected signals from their low-rate samples.

#### B. Contributions

This work extends the FDBF framework to plane-wave imaging, expanding on the initial results we presented in [26]. In particular, we provide a detailed theoretical derivation of the proposed method and show experimental results including both phantom and *in vivo* acquisitions. We also consider the combination of FDBF and  $\ell_1$ -based recovery for sub-Nyquist processing and its use for B-mode and elastography.

Besides the adjustment to the geometry of plane-wave transmissions, dynamic aperture and apodization are introduced to FDBF and implemented directly in frequency. The importance of the dynamic aperture in plane-wave imaging stems from the fact that a relatively shallow depth is of interest. In the far field, the lateral resolution is improved as the aperture increases, while under near-field conditions, the opposite occurs. Dynamic focusing approximately brings far-field conditions to the near field, rendering the large aperture beneficial to all ranges. However, at ranges smaller than the size of the physical aperture of the transducer, which is typically the case for plane-wave imaging, it is challenging to maintain focus even with digital dynamic focusing. As a result, the optimal aperture size varies and should be increased dynamically with the range [27]. Dynamic aperture ensures a constant F-number, denoted  $f\#$ , defined as the depth of focus in the tissue divided by the aperture width. This results in a more homogeneous beam pattern throughout the entire image depth. In this case, the apodization applied to improve contrast by reducing the side lobes of the resulting beam pattern is also dynamic. Explicitly, the window function used for weighting the transducer elements increases dynamically with the range.

Since in Fourier-domain processing, we do not have access to the time samples of the detected signals, we apply dynamic aperture and apodization on frequency samples. To this end, we first express the aperture and apodization as time-dependent weight functions multiplying each detected signal. We then apply them directly in frequency through appropriate modification of the distortion function. As shown in [20] and [22], an efficient implementation of FDBF is obtained through an appropriate approximation, which relies on the decay property of the distortion function. We verify numerically that this is retained in plane-wave imaging with dynamic aperture and apodization, and study the performance of FDBF for different approximation levels.

Translation of beamforming into the frequency domain allows sampling and processing signals at their effective Nyquist rate, which implies a fourfold rate reduction. We next apply sub-Nyquist processing when only a portion of the beam's bandwidth is obtained by FDBF. This implies tenfold rate reduction compared with the minimal rate required for time-domain beamforming. To compensate for the lack of frequency data, we rely on the assumption that a typical ultrasound image is relatively sparse or compressible, namely, comprised of a small number of strong reflectors and much weaker subwavelength scatterers in the scanned tissue. The recovery in this case is formulated as an  $\ell_1$  optimization problem that

is solved using CS methods. The performance is evaluated in terms of contrast and spatial resolution, where we use scans of a tissue mimicking phantom obtained by a commercial Aixplorer scanner. The application of the proposed method on *in vivo* carotid and thyroid scans allows for qualitative evaluation and visual comparison of images obtained using standard processing and FDBF with a tenfold rate reduction. Finally, we perform shear-wave elastography (SWE) [2] using the data obtained by sub-Nyquist FDBF, demonstrating the potential for low-rate velocity estimation.

We note that CS reconstruction in time and frequency for plane-wave imaging was recently studied by several groups to reduce the number of transducers, the number of transmitted plane-waves, and to improve the image quality. In particular, a Fourier-domain formulation of Green's function combined with CS recovery is presented in [28] and is shown to improve the image quality for a single plane-wave transmission. In [29], time-domain compressive beamforming is used to reconstruct point reflectors from a reduced number of receiving elements. Besson *et al.* [30] consider the limited diffraction beam theory [31], [32] applied to plane-wave acquisition in order to compute nonuniform frequency samples of an underlying image. Image reconstruction from its nonuniform spectrum is viewed as an ill-posed inverse problem, while solving it using CS leads to notable improvement in the image quality. In contrast to the above works, we aim at reducing the amount of data required to obtain a clinically meaningful image. To this end, we exploit the ability of CS to recover a signal from its low-rate measurements.

The rest of this paper is organized as follows. In Section II, we review the processing performed in plane-wave imaging. In Section III, we derive the proposed frequency-domain formulation and verify its performance. Sub-Nyquist processing and sparsity-based recovery are presented in Section IV.

## II. COHERENT PLANE-WAVE COMPOUNDING

In coherent plane-wave compounding, the final image is a result of coherently adding several images obtained by transmitting tilted plane-waves with different angles [3]. We begin with a description of beamforming applied upon reception to obtain each one of the images being compounded and then discuss the required computational load.

### A. Time-Domain Processing

Assume that we transmit a plane-wave with an inclination  $\alpha$ , as shown in Fig. 1. An echo reflected by a scatterer positioned at  $(x_f, z)$  arrives at a transducer element placed at  $x_m$  at time

$$\tau_m(z; x_f, \alpha) = \frac{1}{c} (z \cos \alpha + x_f \sin \alpha + \sqrt{z^2 + (x_m - x_f)^2}). \quad (1)$$

Beamforming involves averaging the signals detected by  $M$  transducer elements,  $\{\varphi_m^\alpha(t)\}_{m=1}^M$ , while compensating for the differences in the arrival time. This results in a signal containing the energy reflected from the point  $(x_f, z)$ . Using (1) and

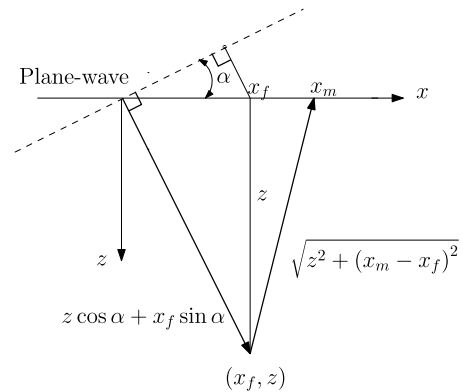


Fig. 1. Plane-wave imaging setup: a transducer is aligned along the x-axis transmitting a propagating plane-wave with inclination  $\alpha$ .

substituting  $z = (ct/2)$ , the beamformed signal, corresponding to an image line at the lateral position  $x_f$ , is given by

$$\Phi(t; x_f, \alpha) = \sum_{m=1}^M w_m(t; x_f) \hat{\varphi}_m(t; x_f, \alpha) \quad (2)$$

where

$$\begin{aligned} \hat{\varphi}_m(t; x_f, \alpha) &= \varphi_m^\alpha(\tau_m(t; x_f, \alpha)) \\ \tau_m(t; x_f, \alpha) &= \frac{1}{2} \left( t \cos \alpha + 2 \frac{x_f}{c} \sin \alpha + \sqrt{t^2 + 4\delta_{fm}^2} \right). \end{aligned} \quad (3)$$

Here,  $\delta_{fm} = |x_m - x_f|/c$  and  $w_m(t; x_f)$  is a time-dependent weight function multiplying each detected signal. Weight functions are introduced to apply dynamic aperture and apodization as will be elaborated on further below. The final image with an improved quality is obtained by coherent summation, so that the  $x_f$ -line in the final image is given by

$$\Phi(t; x_f) = \sum_{\alpha} \Phi(t; x_f, \alpha). \quad (4)$$

As mentioned in Section I, the size of the active aperture,  $M(z)$ , namely, the number of elements contributing to the beamforming summation in (2), should increase dynamically with the range  $z$ . This is done in a way that the ratio between the range and size of the active aperture, denoted by the F-number,  $f\#$ , is constant, ensuring a homogeneous beam pattern throughout the entire image depth. The value of  $f\#$  depends on the array directivity and usually varies between 1 and 2. Lower values of  $f\#$  ensure better focusing [33] but limit the range where  $f\#$  can be kept constant. For a chosen value  $f\#$ , the size of the active aperture as a function of  $z$  is  $M(z) = (z/f\#)$ . Using  $z = (ct/2)$ , we can rewrite  $M(z)$  as a function of time

$$M(t) = \frac{ct}{2f\#}. \quad (5)$$

Thus, for an image line  $x_f$ , the  $m$ th element is active only for

$$|x_m - x_f| \leq \frac{M(t)}{2} \quad (6)$$

i.e., at time  $t \geq 4f\#\delta_{fm}$ .

To improve contrast by reducing side lobes, the active aperture is multiplied by an apodization window. The window

function is dynamically scaled with the range to fit the size of the active aperture. Thus, for an arbitrary apodization function, each element in the active aperture is multiplied by a time-dependent value  $A_m(t; x_f)$ . The overall weight function, including both dynamic aperture and apodization, is given by

$$w_m(t; x_f) = A_m(t; x_f)H(t - 4f\#\delta_{fm}) \quad (7)$$

where  $H(t)$  is a unit step function.

When expressed as a weight function multiplying each detected signal, the dynamic aperture and apodization can be incorporated into FDBF and applied directly in frequency as we will see in Section III.

### B. Computational Load

The beamforming process described in (2) is carried out digitally, rather than by manipulation of the analog signals. The signals detected at each element must be sampled at a sufficiently high rate to apply high-resolution time shifts. In practice, the signal is sampled at rates significantly higher than its Nyquist rate, in order to improve the system's beamforming resolution and to avoid artifacts caused by digital implementation of beamforming in time. Such a beamforming rate,  $f_s$ , usually varies from 4 to 10 times the transducer central frequency [4], [22]. Considering that the effective bandpass bandwidth in medical ultrasound is usually in the order of the central frequency, the detected signals are 4–10 times oversampled compared with the effective Nyquist rate. To avoid confusion, by the effective Nyquist rate, we mean the signal's effective bandpass bandwidth.

Since all the image lines are obtained in parallel, the process described in (2) is performed hundreds of times per plane-wave transmission. Therefore, the computational load is significantly increased compared with standard focused imaging, where each transmission usually requires a single beamforming step. As a result, sampling and processing rate reduction are of high importance in plane-wave imaging.

To reduce the load and promote real-time implementation of ultrafast imaging, we adopt the ideas of beamforming in frequency. As we show, in this domain, the computations can be carried out from less data samples.

## III. FREQUENCY-DOMAIN PROCESSING

To derive the expression for beamforming in frequency using low-rate samples in the plane-wave mode, we need to account for the geometry of plane-wave transmission as well as introduce dynamic aperture and apodization. Explicitly, we show that despite the nonlinear time-dependent nature of beamforming delays and time-dependent weights defined in (2) and (3), the Fourier coefficients of the beam can be computed from the Fourier transform of the detected signals' low-rate samples.

### A. Frequency-Domain Implementation

Following [22], we assume that the support of  $\varphi_m^\alpha(t)$  is contained in  $[0, T)$ , where  $T$  is defined by the transmitted

pulse penetration depth. Hence, the support of  $\Phi(t; x_f, \alpha)$  is limited to  $[0, T_B(x_f))$ , where  $T_B(x_f)$  is defined as

$$T_B(x_f) = \min_{1 \leq m \leq M} \tau_m^{-1}(T; x_f, \alpha) \quad (8)$$

with  $\tau_m^{-1}(t; x_f, \alpha)$  being the inverse of  $\tau_m(t; x_f, \alpha)$ .

Denote the Fourier-series coefficients of  $\Phi(t; x_f, \alpha)$  with respect to the interval  $[0, T)$  by

$$\begin{aligned} c^\alpha[k] &= \frac{1}{T} \int_0^T \Phi(t; x_f, \alpha) I_{[0, T_B(x_f))}(t) e^{-i\frac{2\pi}{T}kt} dt \\ &= \sum_{m=1}^M \hat{c}_m^\alpha[k] \end{aligned} \quad (9)$$

where  $I_{[a,b)}(t)$  is the indicator function, taking the value 1 for  $a \leq t < b$  and 0 otherwise. From (3), we have

$$\begin{aligned} \hat{c}_m^\alpha[k] &= \frac{1}{T} \int_0^T \varphi_m^\alpha(\tau_m(t; x_f, \alpha)) \\ &\quad \times w_m(t; x_f) I_{[0, T_B(x_f))}(t) e^{-i\frac{2\pi}{T}kt} dt. \end{aligned} \quad (10)$$

The idea of FDBF is to obtain frequency components of the beamformed signal without access to its time-domain samples using the Fourier coefficients of nondelayed detected signals. The latter are provided by a low-rate Xampling scheme. We aim, therefore, to derive a relationship between the Fourier coefficients of the beam  $\Phi(t; x_f, \alpha)$  and those of the detected signals. After algebraic manipulation on (10) similar to [20], we obtain

$$\hat{c}_m^\alpha[k] = \frac{1}{T} \int_0^T \varphi_m^\alpha(t) q_{k,m}(t; x_f, \alpha) e^{-i\frac{2\pi}{T}kt} dt. \quad (11)$$

The expression for  $q_{k,m}(t; x_f, \alpha)$  is derived and presented in the Appendix. Note that the delays and weighting of every signal  $\varphi_m^\alpha(t)$  are effectively applied through the distortion function  $q_{k,m}(t; x_f, \alpha)$ .

We next replace  $\varphi_m^\alpha(t)$  by its Fourier coefficients. Denoting the  $n$ th Fourier coefficient by  $c_m^\alpha[n]$ , we can rewrite (11) as

$$\begin{aligned} \hat{c}_m^\alpha[k] &= \sum_n c_m^\alpha[n] \frac{1}{T} \int_0^T q_{k,m}(t; x_f, \alpha) e^{-i\frac{2\pi}{T}(k-n)t} dt \\ &= \sum_n c_m^\alpha[k-n] Q_{k,m;x_f,\alpha}[n] \end{aligned} \quad (12)$$

where  $Q_{k,m;x_f,\alpha}[n]$  are the Fourier coefficients of the distortion function with respect to  $[0, T)$ . When substituted by its Fourier coefficients, the distortion function effectively transfers the beamforming delays defined in (3) as well as dynamic aperture and apodization to the frequency domain. The function  $q_{k,m}(t; x_f, \alpha)$  depends only on the array geometry and is independent of the received signals. Therefore, its Fourier coefficients can be computed offline and used as a lookup table during the imaging cycle.

For apodization in our experiments, we use a normalized Hamming window given by

$$A_m(t; x_f) = \frac{2f\#}{(a^2 + \frac{1}{2}b^2)ct} (a + b \cos(4\pi f\#\delta_{fm}/t)) \quad (13)$$

with  $a = 0.54$  and  $b = 0.46$ . An explicit expression for the resulting distortion function  $q_{k,m}(t; x_f, \alpha)$  for  $\alpha \neq 0$  is given

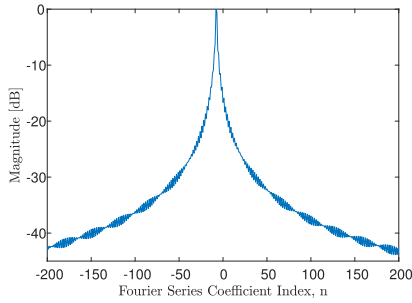


Fig. 2. Illustration of the rapid decay of the Fourier coefficients  $\{Q_{k,m;x_f,\alpha}[n]\}$  of  $q_{k,m}(t;x_f,\alpha)$  around the dc component for Hamming apodization.

in the Appendix. The analytical analysis of this expression is quite involved. Numerical studies show that most of the energy of the set  $\{Q_{k,m;x_f,\alpha}[n]\}$  is concentrated around the dc component. This behavior is typical to any choice of  $k$ ,  $m$ ,  $x_f$ , or  $\alpha$  and is illustrated in Fig. 2. We therefore rewrite (12) with a finite number  $N_q$  of  $Q$ -coefficients as

$$\hat{c}_m^\alpha[k] \simeq \sum_{n=-N_1}^{N_2} c_m^\alpha[k-n] Q_{k,m;x_f,\alpha}[n] \quad (14)$$

where  $N_q = N_2 + N_1 + 1$ . The choice of  $N_1$  and  $N_2$  controls the approximation quality. The dependence of the image quality on  $N_q$  is evaluated and presented in Section III-B for  $N_q = 21, 11$ , and 5.

Substitution of (14) into (9) yields the desired relationship between the Fourier coefficients of the beam and the individual signals

$$c^\alpha[k] \simeq \sum_m \sum_{n=-N_1}^{N_2} c_m^\alpha[k-n] Q_{k,m;x_f,\alpha}[n]. \quad (15)$$

The compounding is then performed directly in frequency

$$c[k] = \sum_\alpha c^\alpha[k] \quad (16)$$

where  $c[k]$  denotes the Fourier coefficients of the  $x_f$ -line in the final image  $\Phi(t;x_f)$  defined in (4). Applying an inverse Fourier transform on  $\{c[k]\}$  yields the beamformed signal in time.

### B. Performance Validation

We verify FDBF on the data acquired by a Supersonic Imagine Aixplorer scanner. The images are produced with a 1-D linear array, model SL 15-4, of 256 elements with a central frequency  $f_c = 9$  MHz and pitch 0.2 mm. Each image was obtained using 41 plane-wave transmissions with a separation of  $1^\circ$ . Standard time-domain processing was performed at the rate of  $f_s = 36$  MHz.

We compare the performance of time-domain processing with the FDBF defined in (11) as well as with the FDBF with different approximation levels in (14) according to the choice of  $N_q$ . The implementation of FDBF using (11) requires the numerical computation of an integral and is not computationally practical. It is provided to verify the similarity between

TABLE I  
ANECHOIC CONTRAST

Method	Contrast, [dB]
Time Domain Beamforming	25.2
FDBF	24.6
FDBF, $N_q = 21$	24.2
FDBF, $N_q = 11$	23.7
FDBF, $N_q = 5$	22.5

time and frequency-domain processing when no approximations are applied. FDBF is performed at the effective bandpass bandwidth of the transmitted signal, which is equal to 9 MHz.

To evaluate spatial resolution, a tissue mimicking the CIRS 040 GSE phantom with wire targets is used. The resulting images are shown in Fig. 3(a). The experimental axial and lateral point spread functions (PSFs) are computed based on the response to a single point target at a depth of 21 mm and are presented in Fig. 4. As can be seen, axial resolution is not affected by the frequency-domain implementation of beamforming for all approximation levels. The lateral resolution is also unchanged; however, the lateral side lobes are slightly higher for a coarse approximation, e.g., with  $N_q = 5$ . As expected, increased lateral side lobes degrade the anechoic contrast computed based on the cyst scans, as shown in Fig. 3(b). The anechoic contrast is defined as

$$CR = \frac{\mu_{\text{cyst}} - \mu_b}{\sqrt{\sigma_{\text{cyst}}^2 + \sigma_b^2}} \quad (17)$$

where  $\mu_{\text{cyst}}$ ,  $\sigma_{\text{cyst}}$ , and  $\mu_b$ ,  $\sigma_b$  stand for the mean and standard deviation of log-compressed values of the cyst and the background, respectively. The computed values are presented in Table I. The contrast obtained by FDBF is 0.6 dB lower than that by time-domain processing. One would expect similar performance for both the methods, since, mathematically, they are completely equivalent. This result can be explained by the fact that the implementation of FDBF according to (11) requires computation of an integral. When performed numerically that such a computation introduces errors that affect the resulting performance. For FDBF with higher values of  $N_q$ , the contrast is still in good agreement with the one obtained by time-domain processing.

In addition, the proposed method is validated with respect to a single beam corresponding to an image line and to the entire image after compounding. To compare the 1-D signals, we calculated the normalized root-mean-square error (NRMSE) between the signals obtained by FDBF and those obtained by standard beamforming in time. Both the classes of signals were compared after envelope detection, performed by a Hilbert transform in order to remove the carrier. Denote by  $\Phi[n;x_f]$  the signal obtained by standard beamforming and let  $\hat{\Phi}[n;x_f]$  denote the signal obtained by beamforming in frequency. The Hilbert transform is denoted by  $\mathcal{H}(\cdot)$ . For the set of  $J$  image lines, we define NRMSE as

$$\text{NRMSE} = \frac{1}{J} \frac{|\mathcal{H}(\Phi[n;x_f]) - \mathcal{H}(\hat{\Phi}[n;x_f])|_2}{\mathcal{H}(\Phi[n;x_f])_{\text{max}} - \mathcal{H}(\Phi[n;x_f])_{\text{min}}} \quad (18)$$

where  $\mathcal{H}(\Phi[n;x_f])_{\text{max}}$  and  $\mathcal{H}(\Phi[n;x_f])_{\text{min}}$  denote the maximal and minimal values of the envelope of the beamformed signal in time.

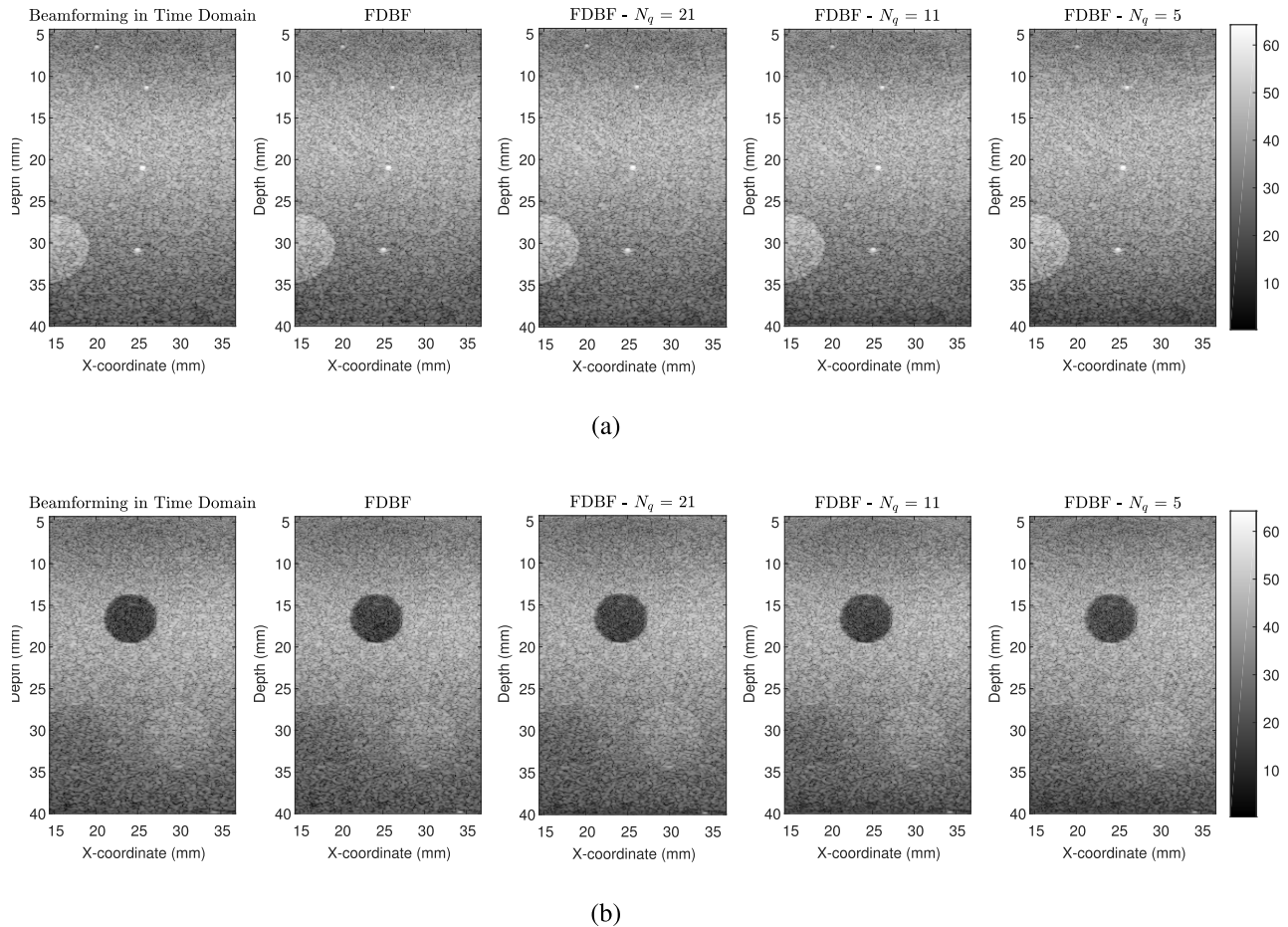


Fig. 3. Comparison of standard time-domain processing and FDBF with different approximation levels. The first column from the left presents time-domain processing while the second one corresponds to FDBF. The last three columns present FDBF with approximation using  $N_q = 21, 11,$  and  $5,$  respectively. (a) Scan of wire targets for resolution evaluation. (b) Scan of anechoic cyst for contrast evaluation.

TABLE II  
NRMSE AND SSIM

Medium	Method	SSIM	NRMSE
Wire targets	FDBF	0.920	0.057
	FDBF, $N_q = 21$	0.918	0.058
	FDBF, $N_q = 11$	0.913	0.060
	FDBF, $N_q = 5$	0.890	0.068
Cyst	FDBF	0.909	0.061
	FDBF, $N_q = 21$	0.900	0.062
	FDBF, $N_q = 11$	0.890	0.065
	FDBF, $N_q = 5$	0.880	0.070

Comparison of the resulting images in Fig. 3 was performed by calculating the structural similarity (SSIM) index [34], commonly used for measuring the similarity between two images. Table II summarizes the resulting values. These values verify that both the 1-D signals and the resulting images are extremely similar, even with a very coarse approximation with only five coefficients.

#### IV. LOW-RATE ACQUISITION AND SUB-NYQUIST PROCESSING

We next address the low-rate acquisition of Fourier coefficients of the detected signals required for frequency-domain processing and show that the beamformed signal can be recovered from its partial frequency data while exploiting its structure.

##### A. Low-Rate Data Acquisition

The low-rate data acquisition step is based on the ideas of Xampling [12], [24], [25], which obtains the Fourier coefficients of individual detected signals from their low-rate samples. More specifically, using Xampling, we can obtain an arbitrary set  $\kappa$ , comprised of  $K$  frequency components, from  $K$  pointwise samples of the signal filtered with an analog kernel  $s(t)$ , designed according to  $\kappa$ . In ultrasound imaging with modulated Gaussian pulses, the transmitted signal has one main band of energy. As a result, the analog filter takes on the form of a bandpass filter, leading to a simple low-rate sampling scheme [22]. The choice of  $\kappa$  dictates the bandwidth of the filter and the resulting sampling rate.

In the plane-wave mode, the same low-rate sampling scheme can be applied to the individual signals detected by the transducer elements yielding their Fourier coefficients. When all the beam's Fourier coefficients within its bandwidth are computed, the sampling and processing rates are equal to the effective Nyquist rate. The beam in time is then obtained simply by an inverse Fourier transform. When further rate reduction is required, only a subset of Fourier coefficients is computed and the beam's structure is exploited to recover it from its partial frequency data.

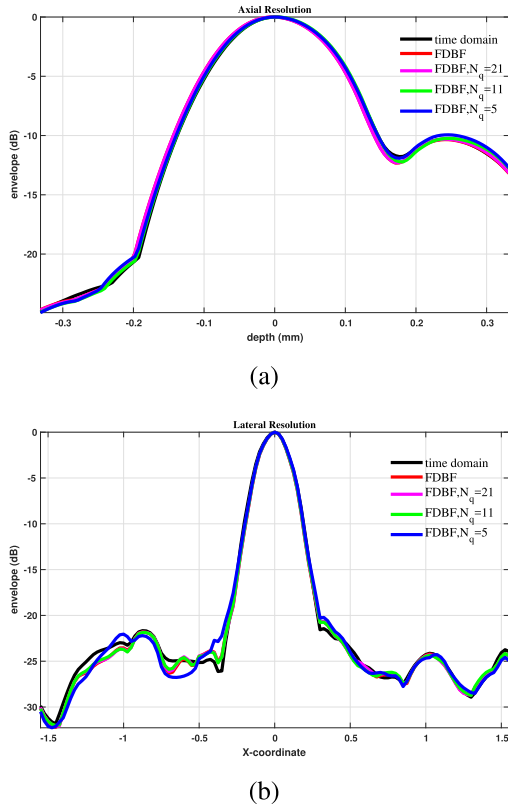


Fig. 4. Spatial resolution comparison for different processing methods. (a) Axial PSF. (b) Lateral PSF. The PSFs are computed empirically based on the response to a single-point target with lateral and axial coordinates [25 mm, 21 mm]. The legend is the same for both (a) and (b).

### B. Sparsity-Based Recovery From Partial Frequency Data

When FDBF is performed at a sub-Nyquist rate, the beamformed signal in time cannot be recovered by an inverse Fourier transform, since only partial frequency information is available. The ideas of sparsity of the beamformed signal combined with  $\ell_1$ -regularized optimization were exploited in [20] and [22]. There, clinical images were recovered from partial frequency data for a focused acquisition mode. In this work, we follow these ideas and compensate for the apparent loss of information of sub-Nyquist processing by relying on the sparsity of the beamformed data.

According to [20], the beamformed signal satisfies the finite rate of innovation (FRI) model [11], [35]. That is, we assume that it can be regarded as a sum of pulses, all replicas of a known transmitted pulse shape

$$\Phi(t; x_f) = \sum_{l=1}^L \tilde{b}_l h(t - t_l). \quad (19)$$

Here,  $h(t)$  is the transmitted pulse,  $L$  is the number of scattering elements in the direction  $x_f$ ,  $\{\tilde{b}_l\}_{l=1}^L$  are the unknown amplitudes of the reflections, and  $\{t_l\}_{l=1}^L$  are the times at which the reflection from the  $l$ th scatterer arrives at the reference element.

Having acquired the Fourier coefficients  $c[k]$  as described in Section III, we now wish to reconstruct the beamformed

signal. Since the beam satisfies the FRI model, our task is to extract the unknown parameters,  $\{\tilde{b}_l\}_{l=1}^L$  and  $\{t_l\}_{l=1}^L$ , that describe it.

Denote  $T_s = (1/f_s)$  and  $N = T/T_s$ . As shown in [22], when the delays  $\{t_l\}_{l=1}^L$  are quantized with a step size  $T_s$ , such that  $t_l = q_l T_s$  for some integer  $0 \leq q_l \leq N - 1$ , the Fourier coefficients of  $\Phi(t; x_f)$  are given by

$$\begin{aligned} c[k] &= \frac{1}{T} \int_0^T \Phi(t; x_f) e^{-i\frac{2\pi}{T}kt} dt \\ &= h[k] \sum_{j=0}^{N-1} b_j e^{-i\frac{2\pi}{N}kj}. \end{aligned} \quad (20)$$

Here,  $h[k]$  is the  $k$ th Fourier coefficient of  $h(t)$  and  $b_j = \tilde{b}_l \delta_{j,q_l}$ , where  $\delta_{a,b}$  is the Kronecker delta.

We conclude that recovering the beamformed signal in time is equivalent to determining  $b_l$  in (20) for  $0 \leq l \leq N - 1$ . In vector-matrix notation, (20) can be rewritten as

$$\mathbf{c} = \mathbf{H}\mathbf{D}\mathbf{b} = \mathbf{A}\mathbf{b} \quad (21)$$

where  $\mathbf{c}$  is a vector of length  $K$  with the  $k$ th entry  $c[k]$ ,  $\mathbf{H}$  is a  $K \times K$  diagonal matrix with the  $k$ th entry  $h[k]$ ,  $\mathbf{D}$  is a  $K \times N$  matrix whose rows are taken from the  $N \times N$  DFT matrix corresponding to the relevant Fourier indices of  $\Phi(t; x_f)$ , and  $\mathbf{b}$  is a column vector of length  $N$  with the  $l$ th entry  $b_l$ .

To extract the values of  $\mathbf{b}$ , which fully describe the beamformed signal, we rely on the assumption that a typical ultrasound image is relatively sparse or compressible. Namely, it is comprised of a small number of strong reflectors and much weaker subwavelength scatterers in the scanned tissue. Using this sparsity assumption, we then find  $\mathbf{b}$  by solving an  $\ell_1$  optimization problem

$$\min_{\mathbf{b}} \|\mathbf{b}\|_1 \quad \text{s.t.} \quad \|\mathbf{A}\mathbf{b} - \mathbf{c}\|_2 \leq \varepsilon. \quad (22)$$

In practice, we solve (22) using the NESTA algorithm [36], which works well when the signal of interest has a high dynamic range. NESTA uses a single smoothing parameter,  $\mu$ , selected based on a tradeoff between the accuracy and the speed of convergence. We choose this parameter empirically to achieve good performance with respect to the image quality.

### C. Results

1) *In Vitro*: To verify the performance of our sub-Nyquist technique, we processed the data at the rate of 3.6 MHz, which corresponds to 0.4 of the effective Nyquist rate and is 10 times lower than the minimal rate required for time-domain beamforming. The processing rate is chosen empirically to be as low as possible while allowing to recover meaningful images. In the context of Xampling, defined in Section IV-A, the chosen processing rate corresponds to an analog pre-processing filter with a bandwidth of 3.6 MHz centered around the central frequency of the transducer,  $f_c = 9$  MHz. All the images are obtained with 41 transmitted plane waves, as described in Section III-B. Spatial resolution is evaluated based on the wire targets' scan presented in Fig. 5. The axial and lateral PSFs, computed based on a point target 21 mm, are presented in Fig. 6. Contrast, evaluated

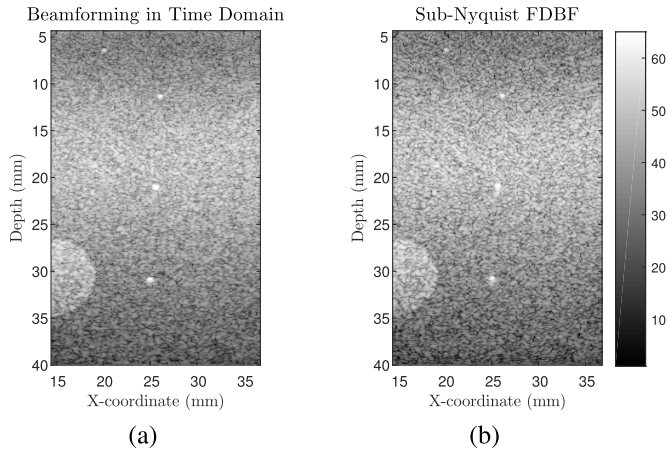


Fig. 5. Scan of wire targets for resolution evaluation. (a) Time-domain beamforming, processed at 36 MHz. (b) Sub-Nyquist FDBF, processed at 3.6 MHz.

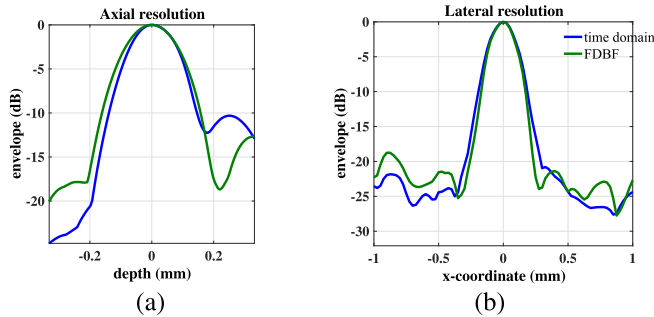


Fig. 6. Spatial resolution comparison for time-domain processing and sub-Nyquist FDBF. (a) Axial PSF. (b) Lateral PSF. The PSFs are computed empirically based on the response to a single-point target with lateral and axial coordinates [25 mm, 21 mm]. The legend is the same for both (a) and (b).

TABLE III  
SUB-NYQUIST FDBF: NRMSE AND SSIM

Medium	SSIM	NRMSE
Wire targets	0.844	0.06
Cyst	0.796	0.08
Carotid ( <i>in vivo</i> )	0.764	0.07
Thyroid ( <i>in vivo</i> )	0.803	0.07

based on the cyst scans shown in Fig. 7, is in good agreement for both the methods. Corresponding values of NRMSE and SSIM are reported in the first two lines of Table III. These values validate a close similarity between the FDBF and the sub-Nyquist FDBF. However, in this case, NRMSE is slightly higher and SSIM is lower than the values obtained in Section III.

2) *In Vivo*: We next applied the sub-Nyquist FDBF to *in vivo* carotid artery data, obtained by scanning a healthy volunteer. The examination of the carotid wall is a powerful tool for atherosclerosis diagnosis and ultrasound imaging is one of the best methods for the evaluation of the wall structure [37]. Intima-media (IM), defined as a double-line pattern on both the walls of the carotid artery, is a structure of interest for diagnosis. It can be seen from the comparison of the highlighted boxes in Fig. 8(a) and (b) that IM is preserved

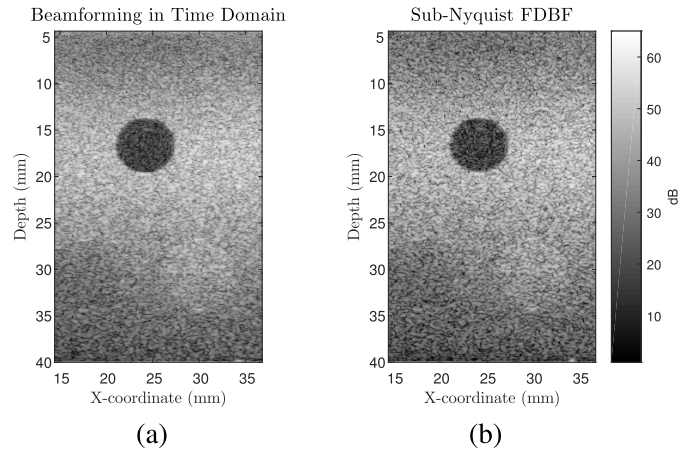


Fig. 7. Scan of an anechoic cyst for contrast evaluation. (a) Time-domain beamforming, processed at 36 MHz, with anechoic contrast 25.2 dB. (b) Sub-Nyquist FDBF, processed at 3.6 MHz, with anechoic contrast 24.8 dB.

by FDBF and can be used for further diagnosis. Moreover, we note that despite a slight degradation of axial resolution, which can be noticed in Fig. 6(a), the *in vivo* image retains all the fine details. This can be explained by the fact that the underlying clinical image contains fewer strong reflectors, and thus better fits the sparsity model.

We verify the ability of (22) to capture speckle by applying the sub-Nyquist FDBF to *in vivo* data, obtained by scanning a healthy volunteer at the thyroid region. The scanned area includes a soft tissue with almost no strong reflectors and, thus, is expected to provide an image comprised of fully developed speckle. The resulting images, shown in Fig. 9(a) and (b), demonstrate a high similarity in the pattern resulting from time and frequency-domain processing. An example of an RF image line obtained by both the methods is presented in Fig. 10. It can be seen that the RF lines are very close even in the regions with weak echoes that are expected to be speckle.

To provide statistical evidence that the resulting pattern is indeed speckle, we check whether it obeys a Rayleigh probability density function [38], [39] by performing a Kolmogorov–Smirnov (K-S) test. This is a common statistical hypothesis test that verifies whether there is enough evidence in the data to deduce that the hypothesis under consideration is correct. To this end, the envelope data of each image is divided into overlapping patches of  $20 \times 15$  pixels and the K-S test is applied to each patch. The patches that pass the K-S test with a significance level  $\alpha = 0.05$  are included into the speckle region of each image. Fig. 9(c) and (d) presents the speckle regions obtained by time-domain beamforming and sub-Nyquist FDBF, respectively. The patches that did not pass the test are zeroed out. As expected, most of the image in Fig. 9(a) is indeed speckle. The speckle region in the image obtained by sub-Nyquist FDBF is in a good agreement with that by time-domain processing. To quantify this similarity, we define the speckle region of time-domain processing as a reference and compute which percentage of it is defined as speckle in an image obtained by the proposed method. The correspondence between the speckle regions in

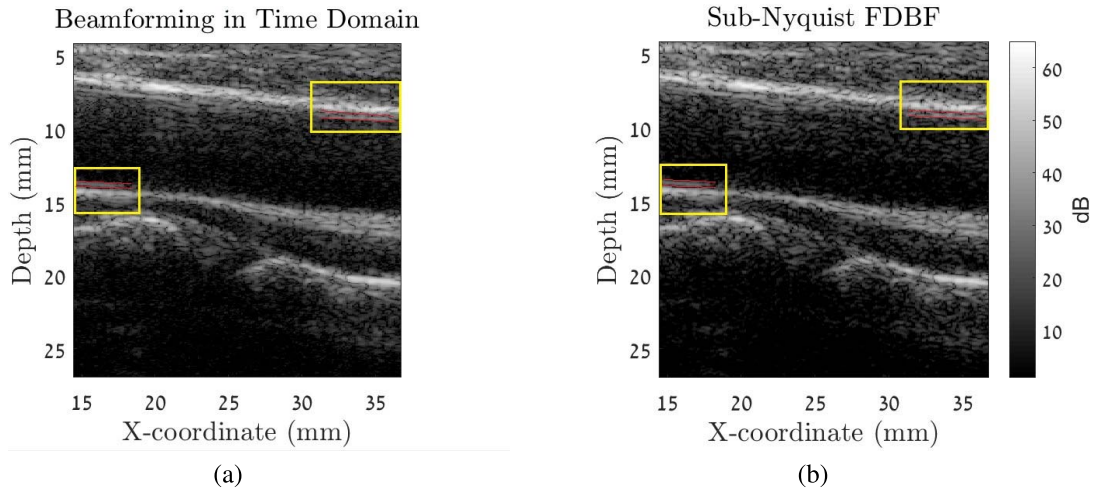


Fig. 8. *In vivo* carotid scan. The highlighted boxes contain the IM regions. (a) Time-domain beamforming, processed at 36 MHz. (b) Sub-Nyquist FDBF, processed at 3.6 MHz.

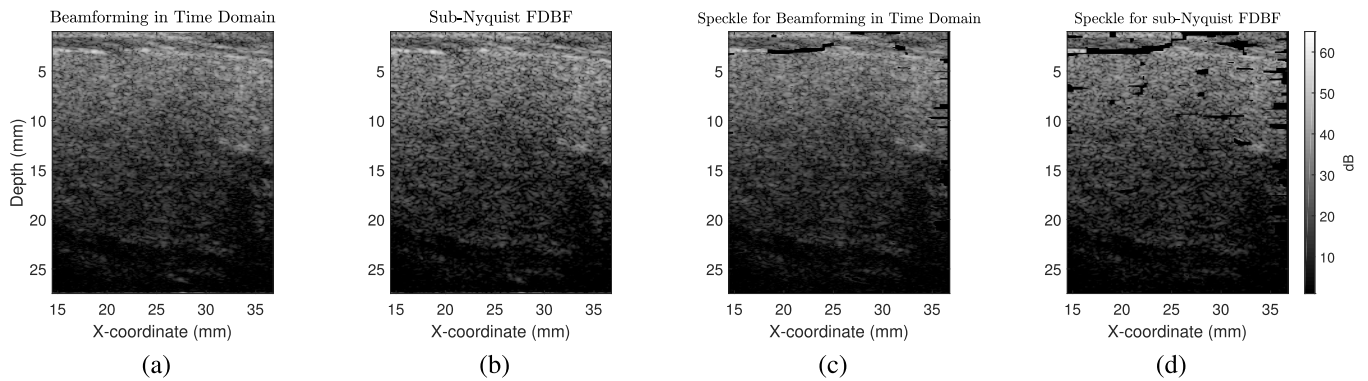


Fig. 9. *In vivo* thyroid scan. (a) Time-domain beamforming, processed at 36 MHz. (b) Sub-Nyquist FDBF, processed at 3.6 MHz. (c) Speckle regions according to the K-S test for time-domain processing at 36 MHz. (d) Speckle regions according to the K-S test for time-domain processing at 3.6 MHz.

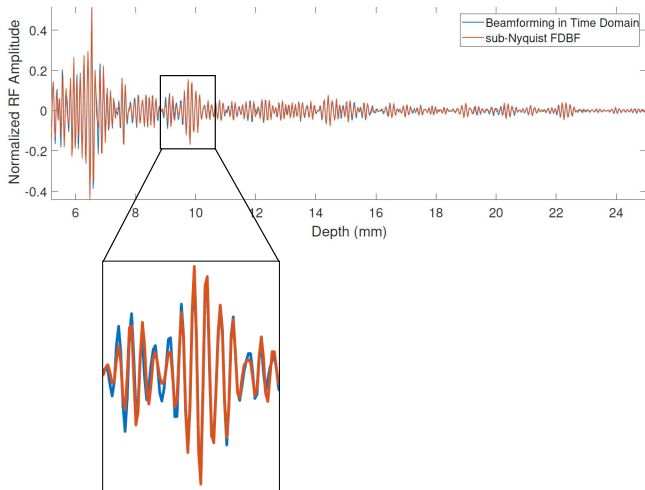


Fig. 10. Comparison of RF lines located at  $x = 27$  mm from the thyroid scan presented in Fig. 9 obtained by time-domain processing and sub-Nyquist FDBF.

Fig. 9(c) and (d) is 95.7%, which clearly shows the ability of sub-Nyquist FDBF combined with an  $\ell_1$ -based prior to recover speckle patterns.

The last two lines of Table III report the values of NRMSE and SSIM, which correspond to applying sub-Nyquist FDBF on *in vivo* carotid and thyroid data, showing similar results to those obtained using the phantom scans. We emphasize that the values of NRMSE and SSIM are provided to give a sense of performance of the proposed method compared with the established technique of time-domain beamforming. In practice, validation is typically performed visually by sonographers, radiologists, and physicians. Furthermore, since our approach uses only a small portion of the spectrum, it inherently filters out the noise that is spread over the entire spectrum. Thus, a high similarity with beamforming in time may not necessarily be advantageous.

3) *Elastography*: We next demonstrate the applicability of sub-Nyquist FDBF to velocity estimation. In particular, we consider supersonic shear imaging [2], where an Aixplorer system was used to scan a CIRS 040GSE phantom with an elasticity target of 40 kPa and 0-dB grayscale compared with the background. Three steered plane waves were used for imaging and sub-Nyquist FDBF was applied on the data acquired for each of them. Inclusion detection was performed using the shear compound, as described in [2], and the resulting elasticity maps are presented in Fig. 11. As can be seen,

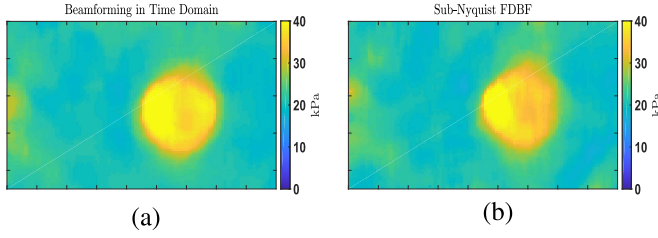


Fig. 11. Elasticity maps of a phantom containing 6-mm hard inclusion. (a) Time-domain beamforming, processed at 30 MHz. (b) Sub-Nyquist FDBF, processed at 5 MHz.

the elasticity maps generated using time-domain beamforming and sub-Nyquist FDBF are similar and allow distinguishing the elasticity target. Using sub-Nyquist FDBF, the data are processed at the rate of 5 MHz, which is six times lower than the rate of 30 MHz, required by time-domain beamforming. This shows the potential use of sub-Nyquist FDBF for velocity estimation.

## V. DISCUSSION AND CONCLUSION

In this work, we extended the FDBF framework developed recently for focused imaging to plane-wave imaging and showed that the core of FDBF, the relationship between the beam and the detected signals in the frequency domain, holds. By appropriate modification of the distortion function that was originally derived for a focused mode to translate the beamforming delays to frequency, we extended FDBF to include dynamic aperture and apodization, crucial for image quality improvement. The efficient implementation of FDBF is enabled by approximation based on the decay properties of the distortion function. Here, we verify numerically that the decay property is preserved in the case of Hamming apodization and evaluate the performance of FDBF for different approximation levels. Such a numerical study can be performed for any choice of the apodization function.

The effect of approximation on the image quality is studied by measuring spatial resolution and contrast as well as the SSIM and NRMSE values using real data acquired by a commercial scanner. The results verify the equivalence of time and frequency-domain processing. We show that FDBF provides four times rate reduction by avoiding oversampling required by the digital implementation of beamforming in time.

When the signal's structure is exploited, further rate reduction is obtained. In this case, we compute only a portion of the beam's bandwidth, which implies sampling and processing the detected signals at a sub-Nyquist rate. The recovery of the beam from its partial frequency data is then performed by solving an optimization problem under the assumption that the signal is compressible. The performance of sub-Nyquist processing is verified in terms of spatial resolution and contrast. Despite the slight degradation in the axial resolution observed in measuring the PSF based on a tissue mimicking phantom, the comparison of *in vivo* carotid scans shows high similarity and the ability of the proposed method to recover the speckle pattern is verified using an *in vivo* thyroid scan.

In addition, we demonstrate the use of sub-Nyquist FDBF to SWE. The ability to achieve significant rate reduction using sub-Nyquist FDBF while obtaining meaningful elasticity maps is of great importance, since SWE is one of the main applications of ultrafast imaging.

Besides the immediate advantage of sampling and processing rate reduction, the proposed method offers two additional benefits. First, the reduction in the number of samples taken at each transducer element is a potential enabler for the concept of a wireless probe and remote processing [9]. Second, FDBF can efficiently incorporate pulse compression required for coded excitation imaging [40], [41]. Transmission of coded signals, such as linear-frequency-modulated chirps, yields an increased SNR and penetration depth, and was shown to improve the performance of shear-wave detection with plane-wave imaging [42].

## APPENDIX DISTORTION FUNCTION

To derive an expression for the distortion function, we consider two cases.

1)  $\alpha = 0$ : In this case, we have

$$\tau_m(t; x_f, 0) = \frac{1}{2}(t + \sqrt{t^2 + 4\delta_{fm}^2}). \quad (23)$$

Defining  $t' = \tau_m(t; x_f, 0)$ , we obtain

$$\begin{aligned} t &= t' - \frac{\delta_{fm}^2}{t'} \\ dt &= \left(1 + \frac{\delta_{fm}^2}{t'^2}\right) dt'. \end{aligned} \quad (24)$$

Using (24), we can write

$$\begin{aligned} \varphi_m^0(\tau_m(t; x_f, 0)) &= \varphi_m^0(t') \\ w_m(t; x_f) &= w_m\left(t' - \frac{\delta_{fm}^2}{t'}; x_f\right) \\ e^{-i\frac{2\pi}{T}kt} &= e^{i\frac{2\pi}{T}k\frac{\delta_{fm}^2}{t'}} e^{-i\frac{2\pi}{T}kt'} \\ I_{[0, T_B(x_f)]}(t) &= I_{[\delta_{fm}, T'_B(x_f; 0)]}(t') \end{aligned} \quad (25)$$

where  $T'_B(x_f; 0) \triangleq \tau_m(T_B(x_f); x_f, 0)$ . Substituting  $t' = \tau_m(t; x_f, 0)$  into (10) yields

$$\hat{c}_m^0[k] = \frac{1}{T} \int_{\delta_{fm}}^{\tau_m(T; x_f, 0)} \varphi_m^0(t') q_{k,m}(t'; x_f, 0) e^{-i\frac{2\pi}{T}kt'} dt' \quad (26)$$

where  $q_{k,m}(t'; x_f, 0)$  is defined in (27), as shown at the top of the next page. By construction,  $T'_B(x_f; 0) \leq T$ . Hence, considering the contribution of  $I_{[\delta_{fm}, T'_B(x_f; 0)]}(t')$ , we can change the bounds of integration in (26) to get

$$\hat{c}_m^0[k] = \frac{1}{T} \int_0^T \varphi_m^0(t') q_{k,m}(t'; x_f, 0) e^{-i\frac{2\pi}{T}kt'} dt'. \quad (28)$$

Omitting the tag superscript in  $t'$ , for clarity, results in (11) where  $\alpha = 0$ .

$$q_{k,m}(t'; x_f, 0) \triangleq w_m \left( t' - \frac{\delta_{fm}^2}{t'}; x_f \right) \cdot I_{[\delta_{fm}, T'_B(x_f; 0)]}(t') \cdot \left( 1 + \frac{\delta_{fm}^2}{t'^2} \right) \cdot \exp \left\{ i \frac{2\pi}{T} k \frac{\delta_{fm}^2}{t'} \right\} \quad (27)$$

$$q_{k,m}(t'; x_f, \alpha) \triangleq w_m \left( \frac{-y \cos \alpha + \sqrt{y^2 - 4\delta_{fm}^2 \sin^2 \alpha}}{\sin^2 \alpha}; x_f \right) \cdot I_{\left[ \frac{x_f \sin \alpha}{c} + \delta_{fm}, T'_B(x_f; \alpha) \right]}(t') \cdot \frac{2(y - t' \cos \alpha)}{\sqrt{y^2 - 4\delta_{fm}^2 \sin^2 \alpha}} \cdot \exp \left\{ i \frac{2\pi}{T} k \left( \frac{-y \cos \alpha + \sqrt{y^2 - 4\delta_{fm}^2 \sin^2 \alpha}}{\sin^2 \alpha} + t' \right) \right\} \quad (31)$$

$$q_{k,m}(t; x_f, \alpha) = \frac{2f\#}{c(a^2 + 0.5b^2)} \cdot \frac{\sin^2 \alpha}{-y \cos \alpha + \sqrt{y^2 - 4\delta_{fm}^2 \sin^2 \alpha}} \cdot \left[ a + b \cos \left( \frac{4\pi f\# \delta_{fm} \sin^2 \alpha}{-y \cos \alpha + \sqrt{y^2 - 4\delta_{fm}^2 \sin^2 \alpha}} \right) \right] \cdot \frac{2}{\sin^2 \alpha} \left[ \frac{y}{\sqrt{y^2 - 4\delta_{fm}^2 \sin^2 \alpha}} - \cos \alpha \right] \cdot \exp \left\{ -i \frac{2\pi}{T} k \frac{-y \cos \alpha + \sqrt{y^2 - 4\delta_{fm}^2 \sin^2 \alpha}}{\sin^2 \alpha} \right\} \cdot \exp \left\{ -i \frac{2\pi}{T} kt \right\} \cdot H \left( \frac{-y \cos \alpha + \sqrt{y^2 - 4\delta_{fm}^2 \sin^2 \alpha}}{\sin^2 \alpha} - 4f\#\delta_{fm} \right) \quad (32)$$

2)  $\alpha \neq 0$ : Define  $t' = \tau_m(t; x_f, \alpha)$  and let  $y = 2(t' - (x_f \sin \alpha / c))$ . We then obtain

$$t = \frac{-y \cos \alpha + \sqrt{y^2 - 4\delta_{fm}^2 \sin^2 \alpha}}{\sin^2 \alpha} \quad (29)$$

$$dt = \frac{2(y - t' \cos \alpha)}{\sqrt{y^2 - 4\delta_{fm}^2 \sin^2 \alpha}} dt'.$$

Substituting the latter into (10), we have

$$\hat{c}_m^\alpha[k] = \frac{1}{T} \int_{\frac{x_f \sin \alpha}{c} + \delta_{fm}}^{\tau_m(T; x_f, \alpha)} \varphi_m^\alpha(t') q_{k,m}(t'; x_f, \alpha) e^{-i \frac{2\pi}{T} kt'} dt' \quad (30)$$

where  $q_{k,m}(t'; x_f, \alpha)$  is given by (31), as shown at the top of this page, and we define  $T'_B(x_f; \alpha) \triangleq \tau_m(T_B(x_f); x_f, \alpha)$ . An explicit expression of the distortion function for Hamming window apodization, defined in (13), is presented in (32), as shown at the top of this page. As in the previous case, it holds that  $T'_B(x_f; \alpha) \leq T$ . Considering the indicator function  $I_{[\frac{x_f \sin \alpha}{c} + \delta_{fm}, T'_B(x_f; \alpha)]}(t')$ , we can modify (30) to get (11).

#### ACKNOWLEDGMENT

The authors would like to thank Prof. M. Fink for many insightful discussions.

#### REFERENCES

- [1] L. Sandrin, S. Catheline, M. Tanter, X. Hennequin, and M. Fink, "Time-resolved pulsed elastography with ultrafast ultrasonic imaging," *Ultrason. Imag.*, vol. 21, no. 4, pp. 259–272, Oct. 1999.
- [2] J. Bercoff, M. Tanter, and M. Fink, "Supersonic shear imaging: A new technique for soft tissue elasticity mapping," *IEEE Trans. Ultrason., Ferroelectr., Freq. Control*, vol. 51, no. 4, pp. 396–409, Apr. 2004.
- [3] G. Montaldo, M. Tanter, J. Bercoff, N. Benech, and M. Fink, "Coherent plane-wave compounding for very high frame rate ultrasonography and transient elastography," *IEEE Trans. Ultrason., Ferroelectr., Freq. Control*, vol. 56, no. 3, pp. 489–506, Mar. 2009.
- [4] B. D. Steinberg, "Digital beamforming in ultrasound," *IEEE Trans. Ultrason., Ferroelectr., Freq. Control*, vol. 39, no. 6, pp. 716–721, Nov. 1992.
- [5] O. D. Grace and S. P. Pitt, "Sampling and interpolation of bandlimited signals by quadrature methods," *J. Acoust. Soc. Amer.*, vol. 48, no. 6A, pp. 1311–1318, 1970.
- [6] J. Ophir *et al.*, "Elastography: Ultrasonic estimation and imaging of the elastic properties of tissues," *Proc. Inst. Mech. Eng., H, J. Eng. Med.*, vol. 213, no. 3, pp. 203–233, 1999.
- [7] M. Tanter and M. Fink, "Ultrafast imaging in biomedical ultrasound," *IEEE Trans. Ultrason., Ferroelectr., Freq. Control*, vol. 61, no. 1, pp. 102–119, Jan. 2014.
- [8] M. Omidyeganeh, Y. Xiao, M. O. Ahmad, and H. Rivaz, "Estimation of strain elastography from ultrasound radio-frequency data by utilizing analytic gradient of the similarity metric," *IEEE Trans. Med. Imag.*, vol. 36, no. 6, pp. 1347–1358, Jun. 2017.
- [9] A. Eilam, T. Chernyakova, Y. C. Eldar, and A. Kempinski, "Sub-Nyquist medical ultrasound imaging: En route to cloud processing," in *Proc. Global Conf. Signal Inf. Process. (GlobalSIP)*, Dec. 2013, pp. 1017–1020.
- [10] Y. C. Eldar, *Sampling Theory: Beyond Bandlimited Systems*. Cambridge, U.K.: Cambridge Univ. Press, 2015.
- [11] Y. C. Eldar and G. Kutyniok, *Compressed Sensing: Theory and Applications*. Cambridge, U.K.: Cambridge Univ. Press, 2012.
- [12] R. Tur, Y. C. Eldar, and Z. Friedman, "Innovation rate sampling of pulse streams with application to ultrasound imaging," *IEEE Trans. Signal Process.*, vol. 59, no. 4, pp. 1827–1842, Apr. 2011.
- [13] X. Zhuang, Y. Zhao, Z. Dai, H. Wang, and L. Wang, "Ultrasonic signal compressive detection with sub-Nyquist sampling rate," *J. Sci. Ind. Res.*, vol. 71, no. 3, pp. 195–199, 2012.
- [14] J. Zhou, S. Hoyos, and B. M. Sadler, "Asynchronous compressed beamformer for portable diagnostic ultrasound systems," *IEEE Trans. Ultrason., Ferroelectr., Freq. Control*, vol. 61, no. 11, pp. 1791–1801, Nov. 2014.
- [15] H. Liebgott, R. Prost, and D. Friboulet, "Pre-beamformed RF signal reconstruction in medical ultrasound using compressive sensing," *Ultrasonics*, vol. 53, pp. 525–533, Feb. 2013.

- [16] A. Achim, A. Basarab, G. Tzagkarakis, P. Tsakalides, and D. Kouamé, "Reconstruction of ultrasound RF echoes modeled as stable random variables," *IEEE Trans. Comput. Imag.*, vol. 1, no. 2, pp. 86–95, Jun. 2015.
- [17] G. Tzagkarakis, A. Achim, P. Tsakalides, and J.-L. Starck, "Joint reconstruction of compressively sensed ultrasound RF echoes by exploiting temporal correlations," in *Proc. Int. Symp. Biomed. Imag. (ISBI)*, Apr. 2013, pp. 632–635.
- [18] C. Quinsac, A. Basarab, and D. Kouamé, "Frequency domain compressive sampling for ultrasound imaging," *Adv. Acoust. Vib.*, vol. 2012, Apr. 2012, Art. no. 231317.
- [19] O. Lorintiu, H. Liebgott, M. Alessandrini, O. Bernard, and D. Friboulet, "Compressed sensing reconstruction of 3D ultrasound data using dictionary learning and line-wise subsampling," *IEEE Trans. Med. Imag.*, vol. 34, no. 12, pp. 2467–2477, Dec. 2015.
- [20] N. Wagner, Y. C. Eldar, and Z. Friedman, "Compressed beamforming in ultrasound imaging," *IEEE Trans. Signal Process.*, vol. 60, no. 9, pp. 4643–4657, Sep. 2012.
- [21] M. F. Schiffner and G. Schmitz, "A low-rate parallel Fourier domain beamforming method for ultrafast pulse-echo imaging," in *Proc. Int. Ultrason. Symp. (IUS)*, Sep. 2016, pp. 1–4.
- [22] T. Chernyakova and Y. C. Eldar, "Fourier-domain beamforming: The path to compressed ultrasound imaging," *IEEE Trans. Ultrason., Ferroelectr., Freq. Control*, vol. 61, no. 8, pp. 1252–1267, Aug. 2014.
- [23] A. Burshtein, M. Birk, T. Chernyakova, A. Eilam, A. Kempinski, and Y. C. Eldar, "Sub-Nyquist sampling and Fourier domain beamforming in volumetric ultrasound imaging," *IEEE Trans. Ultrason., Ferroelectr., Freq. Control*, vol. 63, no. 5, pp. 703–716, May 2016.
- [24] K. Gedalyahu, R. Tur, and Y. C. Eldar, "Multichannel sampling of pulse streams at the rate of innovation," *IEEE Trans. Signal Process.*, vol. 59, no. 4, pp. 1491–1504, Apr. 2011.
- [25] E. Baransky, G. Itzhak, N. Wagner, I. Shmuel, E. Shoshan, and Y. Eldar, "Sub-Nyquist radar prototype: Hardware and algorithm," *IEEE Trans. Aerosp. Electron. Syst.*, vol. 50, no. 2, pp. 809–822, Apr. 2014.
- [26] R. Cohen, Y. Sde-Chen, T. Chernyakova, C. Fraschini, J. Bercoff, and Y. C. Eldar, "Fourier domain beamforming for coherent plane-wave compounding," in *Proc. Int. Ultrason. Symp. (IUS)*, Oct. 2015, pp. 1–4.
- [27] C. E. Thomas, "Dynamic array aperture and focus control for ultrasonic imaging systems," U.S. Patent 4 180 790, Dec. 25, 1979.
- [28] M. Schiffner, T. Jansen, and G. Schmitz, "Compressed sensing for fast image acquisition in pulse-echo ultrasound," *Biomed. Eng.*, vol. 57, no. SI-1 Track-B, pp. 192–195, 2012.
- [29] G. David, J.-L. Robert, B. Zhang, and A. F. Laine, "Time domain compressive beam forming of ultrasound signals," *J. Acoust. Soc. Amer.*, vol. 137, no. 5, pp. 2773–2784, 2015.
- [30] A. Besson *et al.*, "A sparse reconstruction framework for Fourier-based plane-wave imaging," *IEEE Trans. Ultrason., Ferroelectr., Freq. Control*, vol. 63, no. 12, pp. 2092–2106, Dec. 2016.
- [31] J.-Y. Lu and J. F. Greenleaf, "Pulse-echo imaging using a nondiffracting beam transducer," *Ultrasound Med. Biol.*, vol. 17, no. 3, pp. 265–281, 1991.
- [32] J.-Y. Lu and J. F. Greenleaf, "Ultrasonic nondiffracting transducer for medical imaging," *IEEE Trans. Ultrason., Ferroelectr., Freq. Control*, vol. 37, no. 5, pp. 438–447, Sep. 1990.
- [33] W. D. O'Brien, Jr., "Ultrasound–biophysics mechanisms," *Prog. Biophys. Mol. Biol.*, vol. 93, nos. 1–3, pp. 212–255, 2007.
- [34] Z. Wang, A. C. Bovik, H. R. Sheikh, and E. P. Simoncelli, "Image quality assessment: From error visibility to structural similarity," *IEEE Trans. Image Process.*, vol. 13, no. 4, pp. 600–612, Apr. 2004.
- [35] M. Vetterli, P. Marziliano, and T. Blu, "Sampling signals with finite rate of innovation," *IEEE Trans. Signal Process.*, vol. 50, no. 6, pp. 1417–1428, Jun. 2002.
- [36] S. Becker, J. Bobin, and E. J. Candès, "NESTA: A fast and accurate first-order method for sparse recovery," *SIAM J. Imag. Sci.*, vol. 4, no. 1, pp. 1–39, 2011.
- [37] I. Simova, "Intima-media thickness: Appropriate evaluation and proper measurement, described," *E-J. ESC Council Cardiol. Pract.*, vol. 13, no. 21, pp. 1–14, 2015.
- [38] C. B. Burckhardt, "Speckle in ultrasound B-mode scans," *IEEE Trans. Sonics Ultrason.*, vol. SU-25, no. 1, pp. 1–6, Jan. 1978.
- [39] R. F. Wagner, S. W. Smith, J. M. Sandrik, and H. Lopez, "Statistics of speckle in ultrasound B-scans," *IEEE Trans. Sonics Ultrason.*, vol. SU-30, no. 3, pp. 156–163, May 1983.
- [40] A. Lahav, Y. Ben-Shalom, T. Chernyakova, and Y. C. Eldar, "Coded excitation ultrasound: Efficient implementation via frequency domain processing," in *Proc. Int. Conf. Acoust., Speech Signal Process. (ICASSP)*, Mar. 2016, pp. 674–678.
- [41] A. Lahav, T. Chernyakova, and Y. C. Eldar, "FoCUS: Fourier-based coded ultrasound," *IEEE Trans. Ultrason., Ferroelectr., Freq. Control*, vol. 64, no. 12, pp. 1828–1839, Dec. 2017.
- [42] P. Song, M. W. Urban, A. Manduca, J. F. Greenleaf, and S. Chen, "Coded excitation plane wave imaging for shear wave motion detection," *IEEE Trans. Ultrason., Ferroelectr., Freq. Control*, vol. 62, no. 7, pp. 1356–1372, Jul. 2015.

**Tanya Chernyakova**, photograph and biography not available at the time of publication.

**Regev Cohen**, photograph and biography not available at the time of publication.

**Rotem Mulayoff**, photograph and biography not available at the time of publication.

**Yael Sde-Chen**, photograph and biography not available at the time of publication.

**Christophe Fraschini**, photograph and biography not available at the time of publication.

**Jeremy Bercoff**, photograph and biography not available at the time of publication.

**Yonina C. Eldar**, photograph and biography not available at the time of publication.